An Organism-Level Quantitative Flux Model of Energy Metabolism in Mice

Bo Yuan [1], Will Doxsey [1], Özlem Tok [1], Young Yon Kwon [1],
Karen E. Inouye [1,2], Gökhan S. Hotamışlıgil [1,2,3], Sheng Hui [1,2,4,*]

[1] Department of Molecular Metabolism, Harvard T. H. Chan School of Public Health, Boston, Massachusetts, USA.
[2] Sabri Ülker Center for Metabolic Research, Department of Molecular Metabolism, Harvard T.H. Chan School of Public Health, Boston, Massachusetts, USA.
[3] Broad Institute of Harvard and MIT, Cambridge, Massachusetts, USA.
[4] Lead Contact
* Correspondence: shui@hsph.harvard.edu (S.H.)

Keywords: isotope tracing, in vivo flux quantification, circulating nutrients, energy metabolism, obesity

Highlights

- A flux model of energy metabolism integrating ^{13}C labeling of metabolites and CO_2
- Circulating nutrients have characteristic partition between oxidation and storage
- Circulating nutrients' total cycling flux outweighs their total oxidation flux
- Cycling fluxes are extensively elevated in ob/ob but not in diet-induced obese mice

26 **Graphical Abstract**

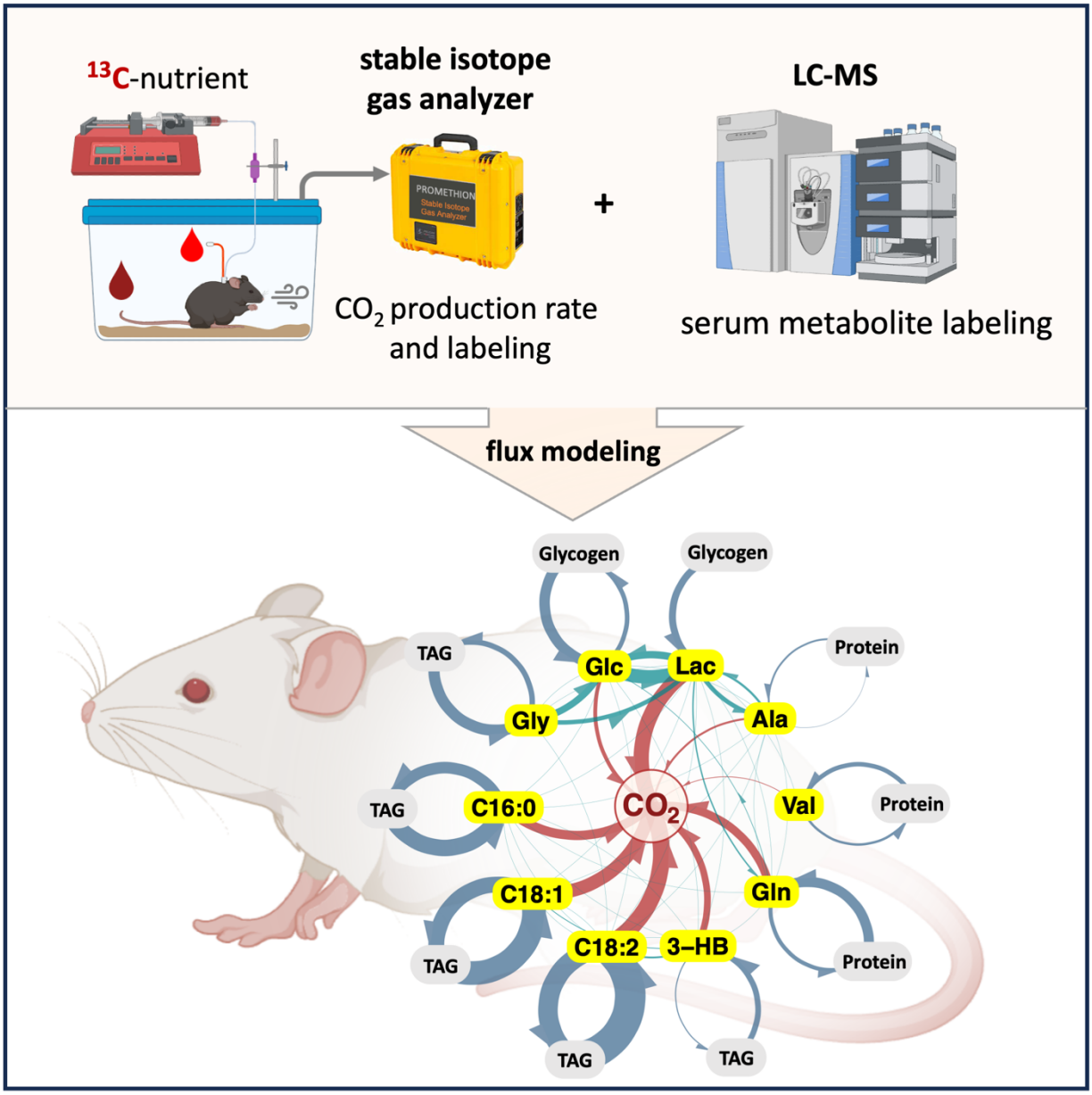

27

Summary

Mammalian tissues feed on nutrients in the blood circulation. At the organism-level, mammalian energy metabolism comprises of oxidation, storage, interconverting, and releasing of circulating nutrients. Though much is known about the individual processes and nutrients, a holistic and quantitative model describing these processes for all major circulating nutrients is lacking. Here, by integrating isotope tracer infusion, mass spectrometry, and isotope gas analyzer measurement, we developed a framework to systematically quantify fluxes through these metabolic processes for 10 major circulating energy nutrients in mice, resulting in an organism-level quantitative flux model of energy metabolism. This model revealed in wildtype mice that circulating nutrients have more dominant metabolic cycling fluxes than their oxidation fluxes, with distinct partition between cycling and oxidation flux for individual circulating nutrients. Applications of this framework in obese mouse models showed on a per animal basis extensive elevation of metabolic cycling fluxes in ob/ob mice, but not in diet-induced obese mice. Thus, our framework describes quantitatively the functioning of energy metabolism at the organism-level, valuable for revealing new features of energy metabolism in physiological and disease conditions.

INTRODUCTION

While our body is ultimately powered by nutrients in the food we eat, our tissues consume nutrients from the blood circulation for their energy needs, mostly by oxidizing them into CO_2. The circulating nutrients are supplied from digestion of food or breakdown of tissue nutrient storages such as glycogen and triacylglycerol (TAG). Instead of following the simple one-way process of release from storage to oxidation by tissues, however, a circulating nutrient can be simultaneously recycled back to its tissue storages, thus forming metabolic cycles (**Figure 1A**). For example, circulating glucose can be released from and resynthesized into tissue glycogen at the same time (Shipley et al., 1967, 1970). Another well-known example is the triacylglycerol-fatty acid cycle, which involves the simultaneous release of non-esterified fatty acid (NEFA) from tissue triacylglycerol (TAG) into circulation and resynthesis of tissue TAG from circulating NEFA (Nye et al., 2008; Randle et al., 1963). In addition to the metabolic fates of oxidation and resynthesis into tissue storage, circulating nutrients also interconvert with each other, forming additional metabolic cycles. One prominent example is the Cori cycle, where circulating glucose is converted into circulating lactate, which is then converted back into circulating glucose through gluconeogenesis (Cori, 1931; Reichard et al., 1963). Thus, circulating nutrients are involved in a complex network of fluxes, including those in oxidation, inter-nutrient metabolic cycling, and nutrient-storage metabolic cycling (**Figure 1A)**. Despite extensive knowledge of some well-known examples, a holistic and quantitative view of these fluxes encompassing all major circulating nutrients is lacking, preventing a global view of how energy metabolism is functioning in health and diseases such as obesity.

Isotope tracing is a powerful approach to determine metabolic fluxes. For a system (e.g., cells, animals) administered with isotope tracers, the isotope labeling of metabolites reflects the fluxes on the underlying metabolism (Fernández-García et al., 2020; Metallo, 2015). Modern analytical methods such as mass spectrometry (MS) and nuclear magnetic resonance (NMR) can generate rich isotope labeling information for many metabolites, allowing systematic flux calculations for multiple metabolic reactions within complex networks (Antoniewicz, 2018; Hasenour et al., 2020). The applications of isotope-based flux analysis has enabled many important discoveries in both in vitro and in vivo models (Befroy et al., 2014; Cappel et al., 2019).

In our previous work, with infusion of isotope-labeled nutrients to mice and mass spectrometry measurement of circulating metabolite labeling, we systematically determined the interconversion fluxes between the major circulating nutrients, revealing sustained metabolic cycling across diets (Hui et al., 2020).

In addition to the classic isotope analysis platform by MS and NMR, isotope-labeled CO_2 tracing provides uniqiue insight of nutrient oxidization. While the tracing of radioactive $^{14}CO_2$ was employed in the previous in vivo flux analysis, it has been done only to a few nutrients, such as glucose (Del Prato et al., 1993) and palmitate (Campbell et al., 1992), and simultaneous labeling measurement for multiple metabolites was restricted. The use of stable $^{13}CO_2$ tracing (McCue and Welch, 2016), on the other hand, makes close integration with the MS measurement a possibility, creating a new yet uncharted revenue of in vivo flux quantification.

Here, we integrated isotope tracer infusion, MS, and $^{13}CO_2$ gas analyzer measurement, and developed a fluxomics framework to calculate the oxidation, inter-nutrient and nutrient-storage fluxes for 10 major circulating nutrients in mice (**Figure S1**). The resulting quantitative flux model at the organism-level revealed many surprising features of mammalian energy metabolism. Of note, metabolic cycling flux is numerically more prominent than oxidation for circulating nutrients, despite the already enormous oxidative flux. To unravel the global changes of energy metabolism in obesity, we applied this framework on obesity models. Among our findings, compared with lean mice and on a per animal basis, the metabolic cycling fluxes of carbohydrate and fat nutrients were elevated by about 2-fold in the leptin-deficient obese mice while they remained largely the same in diet-induced obese mice. Overall, our work provides a framework for building an organism-level flux model of energy metabolism, a useful tool for metabolic research.

RESULTS

Quantifying the Fraction of Oxidation for a Circulating Nutrient

In general, the carbon atoms in a circulating nutrient either leave the body as the oxidation product CO_2 or are recycled back into storages in the body (**Figure 1A**). To quantify these oxidation fluxes and storing fluxes of circulating nutrients, we first aimed to determine what

102 fraction of a circulating nutrient is oxidized into CO_2, or its fraction of oxidation (f_{ox}). For this,
103 using circulating glucose as an example, we intravenously administered a small amount of ^{13}C-
104 uniformly labeled glucose as a single bolus into modestly fasted mice, and monitored the $^{13}CO_2$
105 production using a metabolic cage equipped with a $^{13}CO_2$ analyzer (**Figure 1B**). The production
106 flux of $^{13}CO_2$ peaked at around 30 min, significantly dropped in another 2 hours, and tailed to
107 approach background level within a total of 6 hours (**Figure 1B;** see calculation of $^{13}CO_2$ flux in
108 **Supplementary Note 1**). Integration of the $^{13}CO_2$ production kinetic curve over the 6 hours gives
109 the total $^{13}CO_2$ production from the tracer administered. The recovery was then calculated as the
110 ratio between the total production of $^{13}CO_2$ (µmol) and the administered tracer dose (µmol ^{13}C
111 atoms). Glucose recovery was thus determined to be 0.75. This suggests that 25% of circulating
112 glucose atoms were destined to storage pools, such as triglycerides, proteins, glycogen, and other
113 macromolecules. To verify this number, we intravenously injected the radioactive tracer ^{14}C-
114 glucose into mouse, and measured the remaining radioactivity in the carcass 6 hours after
115 administration. The carcass was digested into a solution, and the radioactivity was measured
116 using a scintillation counter. We detected 26% of the administered dose in the carcass (**Figure**
117 **1C**), consistent with our $^{13}CO_2$ measurement and a previous result (Tolbert et al., 1956).
118 To further confirm the glucose recovery result, instead of a bolus injection of ^{13}C-glucose,
119 we infused ^{13}C-glucose into the mouse systemic circulation via a pre-implanted jugular vein
120 catheter. Compared to the bolus injection, the constant infusion at a low rate reduces the
121 amount of exogenous nutrient per minute administered to the animal and thus minimizes
122 potential perturbation to metabolism. Here the recovery is the ratio of $^{13}CO_2$ production rate
123 (µmol/min) at steady state to the ^{13}C-infusion rate (µmol ^{13}C atoms/min). With this experiment,
124 we measured glucose recovery to be 0.73 (**Figure 1D**), in close agreement with that measured
125 with the bolus administration. We thus combined results from both methods and took the
126 average as the recovery of glucose.
127 To obtain the f_{ox} value for glucose, we next took in account the fact that a portion of the
128 $^{13}CO_2$ generated from oxidation of ^{13}C-glucose can undergo carboxylation and get incorporated
129 into metabolite pools (such as urea and oxaloacetic acid) which are not recovered in the
130 exhalation (Elia et al., 1992). For this, we intravenously infused ^{13}C-labeled bicarbonate, and

131 determined a recovery of 90% for bicarbonate, indicating that 90% of produced CO_2 from
132 substrate oxidation actually leaves the body as exhaled CO_2. We thus took the ratio of glucose
133 recovery to bicarbonate recovery as the glucose f_{ox}, and obtained a value of 0.81 (**Figure 1E**).
134 This value reflects that ~80% of circulating glucose is oxidized, and ~20% is recycled back to
135 storage pools independent of the CO_2 carboxylation pathway.
136
137 **Distinct f_{ox} Values for Different Circulating Nutrients**
138 In addition to glucose, we went on to quantify the f_{ox} for 12 other circulating nutrients (**Figures**
139 **1E**, **S1B-E**). For most circulating nutrients investigated, the f_{ox} by both bolus injection and
140 infusion methods are generally consistent (**Figure S1D**), and we pooled the data from both
141 methods. Glycerol, however, was 30% more oxidized when administered as a bolus than by
142 infusion, suggesting significant perturbation to glycerol metabolism by the bolus administration.
143 Given the negligible perturbation by infusion, we used infusion-based f_{ox} for glycerol for further
144 analyses.
145 Among all 13 circulating nutrients, lactate had the highest f_{ox} of around 100%, significantly
146 higher than glucose f_{ox} of 81% (**Figure 1E**). This result further substantiates circulating lactate's
147 role as an energy source for tissues (Hui et al., 2017). The ketone body 3-hydroxybutyrate and
148 acetate also have high f_{ox} of 81% and 86%, respectively, indicating their main use as energy
149 sources in the body. Non-esterified fatty acids (NEFA) occupy the lower end of the f_{ox} spectrum.
150 Palmitate (C16:O), oleate (C18:1), and linoleate (C18:2), the most abundant NEFAs in circulation,
151 have f_{ox} values of around 45%, suggesting prominent fluxes from circulating NEFAs back to tissue
152 triglycerides (Reshef et al., 2003). The branched-chain amino acid (BCAA) valine has a f_{ox} of only
153 32%, similar to that of BCAA leucine (Tolbert et al., 1956). Together with f_{ox} of 24~26% for the
154 essential amino acids methionine and tryptophan, this result reveals that the majority of
155 proteolysis-released circulating amino acids are recycled back into proteins. In contrast,
156 circulating glutamine and alanine have high f_{ox} of 77% and 84%, respectively, indicating their
157 unique roles in energy metabolism among amino acids. Thus, f_{ox} of a circulating nutrient reveals
158 its main role in mammalian metabolism and is a fundamental property of circulating nutrients.

159 In the following flux analysis, we focused on 10 nutrients in **Figure 1E**, which were the top
160 9 circulatory nutrients (Hui et al., 2017) and valine. Albeit a small circulatory turnover flux, valine
161 was included as a reporter of protein metabolism. The other 9 nutrients are glucose, lactate,
162 glycerol, alanine, glutamine, 3-HB, C16:0, C18:1, and C18:2.
163
164 **Quantifying Oxidation and Storing Fluxes of Circulating Nutrients**
165 Based on the f_{ox} measurement, we next sought to quantify the fluxes associated with oxidation
166 and storing destinies of circulating nutrients. At the steady state of ^{13}C-tracer infusion, we
167 sampled the blood and measured the ^{13}C-labeling of the infused nutrient using mass
168 spectrometry (**Figure 2A**). The serum labeling of the infused nutrient (L) reflects the dilution of
169 the infusate (at infusion rate I) by the endogenous production flux R_a of the nutrient, with $R_a =$
170 $I\frac{1-L}{L}$. The R_a is an important quantity to reflect a nutrient's circulatory turnover, and can be
171 significantly changed at different physiological conditions, such as under hyperinsulinemia
172 (**Figure S2A**) and beta-adrenergic agonism (**Figure S2B**). Since f_{ox} and $1 - f_{ox}$ are the fraction of
173 R_a that is fated to oxidation and storing, respectively (**Figure 2B**), the oxidation and storing fluxes
174 of a circulating nutrient, denoted as J_{OX} and J_S, respectively, can be calculated (see derivation in
175 **Supplementary note 2**) as

$$J_{OX} = R_a f_{ox} \quad (1)$$

$$J_S = R_a(1 - f_{ox}) \quad (2)$$

176 The absolute flux values reveal quantitatively the magnitude of each nutrient as an oxidation
177 substrate or storage precursor (**Figure 2C**). For example, though linoleic acid has lower f_{ox} than
178 glucose (**Figure 1E**), it has higher oxidation flux. Valine has the largest storing fraction ($1 - f_{ox}$),
179 but the associated storing flux is among the smallest.
180
181 **Quantifying *Direct* Oxidation and Storing Fluxes of Circulating Nutrients**
182 The oxidation flux for a circulating nutrient quantified above describes the nutrient's ultimate
183 disposal into CO_2. It includes both direct and indirect oxidation fluxes of the nutrient. The indirect
184 oxidation refers to the process that a circulating nutrient is first converted into other circulating
185 nutrients before being oxidized. For example, an important indirect oxidation route for

circulating glucose is via circulating lactate. In like manner, the storing flux also comprises both the direct and indirect ways. To gain further insights on the sources and sinks of circulating nutrients, we next sought to quantify the *direct* fate of a circulating nutrient to oxidation and storage.

We denote the direct oxidation flux from a circulating nutrient j as O_j, which we aim to calculate. Now consider the steady state of a nonperturbative infusion of a ^{13}C-labeled nutrient, e.g., ^{13}C-glucose. The $^{13}CO_2$ production flux from the animal is given by If_{ox}, where I is the infusion rate and f_{ox} is the glucose fraction of oxidation. As the $^{13}CO_2$ production is also equal to the sum of labeled direct oxidation fluxes from all circulating nutrients, we have

$$\sum O_j^t L_j = If_{ox} \tag{3}$$

where O_j^t is the direct oxidation flux (including both ^{13}C and ^{12}C) of nutrient j, and L_j the labeled fraction of the nutrient (illustrated in **Figure 3A**). As the endogenous unlabeled oxidation flux O_j accounts for $1 - L_j$ fraction of O_j^t, or $O_j = O_j^t(1 - L_j)$, plugging it into the above equation gives the expression with the endogenous oxidation flux O_j as the only unknown

$$\sum \frac{L_j}{1 - L_j} O_j = If_{ox} \tag{4}$$

This equation holds under the infusion of each different ^{13}C-labeled nutrient. As such, the infusion of 10 different ^{13}C-nutrients unveils the inter-labeling pattern among these nutrients (**Figures 3B** and **S3A**), and allows the construction of a linear system of 10 equations of

$$\boldsymbol{A} \cdot \begin{bmatrix} O_1 \\ O_2 \\ \vdots \\ O_{10} \end{bmatrix} = \begin{bmatrix} I_1 f_{ox_1} \\ I_2 f_{ox_2} \\ \vdots \\ I_{10} f_{ox_{10}} \end{bmatrix} \tag{5}$$

where $\boldsymbol{A}$ is a 10×10 matrix, with element $L_j^k/(1 - L_j^k)$ in the kth row and j^{th} column, and L_j^k representing the labeling of jth circulating nutrient under the infusion of the kth tracer. Solving these linear equations yields the direct oxidation fluxes O_j of the circulating nutrients (**Figure 3C**). The direct storing fluxes S_j can be calculated in the same manner (**Figure 3C**; see more details in derivation in **Suppl. Note 3**).

207

208 **Direct Contribution of Circulating Nutrients to Total Energy Expenditure**

209 The direct oxidation fluxes form an organism-level view of burning circulating nutrients for
210 energy (**Figure 3**). Compared with the total CO_2 exhaled by the animal measured directly using a
211 metabolic cage, the 10 nutrients alone accounted for about 80% of the total CO_2 production,
212 confirming that these nutrients represent the top circulating nutrients. Glucose, while being the
213 most famous energy nutrient, has rather minimal direct oxidation flux, accounting for only
214 marginal fraction of total energy expenditure (TEE) (**Figure 3C**). Instead, circulating lactate,
215 mostly derived from glucose, is the dominant carbohydrate that directly fuels oxidation (Hui et
216 al., 2017), responsible for about 20% of TEE. Glutamine, as the single most important amino acid
217 fuel, contributes to 7% of TEE, while alanine and valine contribute 1.5% and 0.7%, respectively.
218 As the oxidative disposal of essential amino acid reflects the use of proteins for energy
219 expenditure, based on the content of valine (5%) in muscle proteins (Gorissen and Phillips, 2018),
220 the direct oxidation of protein-originated amino acids can be estimated to provide approximately
221 14% of TEE (Fearon et al., 1988; Matthews et al., 1980). The ketone body 3-HB contributes to 5%
222 of TEE. Due to the rapid equilibrium between 3-HB and acetoacetate, this quantity reflects the
223 contribution of the total ketone bodies (Keller et al., 1981). The three NEFA species, palmitate,
224 oleate, and linoleate, are among the most prominent fuels, contributing to 8%, 15% and 22% of
225 TEE, respectively, or 45% in sum. As these top 3 NEFAs account for about 75% of total NEFA in
226 circulation (**Figure S3B**), approximately 60% of TEE is supported by the total NEFA in circulation.
227 Glycerol is uniquely the only nutrient that is not directly engaged in oxidation (Hui et al., 2020).
228 All nutrients considered together, using both direct measurement and empirical extrapolation,
229 close to 100% of TEE can be quantitatively accounted for (**Figure 3D**, showing the direct TEE
230 contribution from carbohydrate nutrients (glucose, lactate, and glycerol), NEFAs, protein, and
231 ketone bodies).

232

233 **Recycling to Storage Is a Highly Prominent Fate of Circulating Nutrients**

234 The direct storing fluxes revealed the composition of nutrients for resynthesizing fuel storages.
235 The total NEFAs present a dominating 60% of the total storing flux (**Figure 3D**). Amino acids also

236 have prominent storing fluxes. Using valine as a representative of protein-originated amino acids,
237 the total amino acids storing flux accounts for 30% of the total storing flux. Carbohydrates have
238 a minor part (6%) in the total storing flux, with lactate having zero direct storing flux. This again
239 highlights lactate's role as a fuel metabolite. Most strikingly, all circulating nutrients considered
240 together, the total storing flux is 23% higher than that of oxidation (**Figure 3D**), vividly
241 demonstrating the enormity of futile cycling fluxes of circulating nutrients.
242
243 **Quantifying Inter-converting Fluxes between Circulating Nutrients and their Releasing Fluxes**
244 **from Storages**
245 We have so far focused on oxidation and storing as destinies for circulating nutrients. The
246 storages however also serve as sources for circulating nutrients. To work toward a full view of
247 metabolism of circulating nutrients, here we attempted to quantify the production fluxes of the
248 circulating nutrients from the storage pools. In the same calculation, we also obtained the
249 interconverting fluxes between circulating nutrients, which was a main result in our previous
250 work (Hui, et al. 2020).
251 To illustrate the calculation, we use glucose as an example and quantify its production
252 fluxes, including the storage releasing flux F_S, i.e., glycogenolysis, and the gluconeogenic flux F_j
253 from circulating nutrient j (**Figure 4A**). Now consider the steady state during a nonperturbative
254 ^{13}C-glucose infusion with an infusion rate I. The total glucose production flux (P^{total}) at steady
255 state is equal to summation of all incoming fluxes from different sources to glucose, given by

$$P^{total} = I + \sum_j F_j^t + F_S \tag{6}$$

256 where $F_j^t = \frac{F_j}{1-L_j}$ with L_j the labeling of nutrient j. Note that F_j^t is the total flux from nutrient j
257 to glucose including both endogenous unlabeled flux F_j and labeled flux $F_j^t L_j$. The mass balance
258 of the labeled glucose pool (with the labeling denoted as L_{glc}) requires

$$\sum_j F_j^t L_j + I = P^{total} L_{glc} \tag{7}$$

259 where the left-hand-side is the incoming ^{13}C flux to glucose from different sources, and the right-
260 hand-side the outgoing labeled glucose flux. Eq. (6) and the expression for F_j^t can be plugged into
261 Eq. (7) to form an equation with F_j's and F_S as the only unknowns. Such an equation holds under
262 the infusion of other ^{13}C-nutrients, but with $I = 0$. With infusions of ^{13}C glucose and 9 other ^{13}C-
263 labeled circulating nutrients, a linear system of 10 equations can be then constructed for the 10
264 unknowns including the 9 F_j's and F_S, in like manner as Eq. (4) (see Methods). Solving the
265 equations yielded the storage releasing flux, and the conversion fluxes from the 9 circulating
266 nutrients to produce circulating glucose. In similar fashion, the releasing fluxes and inter-
267 converting fluxes can be calculated for other circulating nutrients using the same computational
268 framework. More derivation details can be found in **Suppl. Note 4**.
269
270 **Sources of Circulating Nutrients**
271 The storage releasing flux and inter-converting flux results calculated above provide a
272 quantitative view of the direct sources for each of the 10 circulating nutrients (**Figure 4B**). Two
273 types of circulating nutrients can be seen, nutrients directly sourced from the storages, and those
274 derived from both storages and other circulating nutrients. NEFA and glycerol are almost
275 exclusively released from the TAG store, and valine and glutamine from the protein store. In
276 contrast, glucose, lactate, alanine, and 3-HB are additionally sourced from other circulating
277 nutrients. For circulating glucose, about 40% is released from glycogen, while the remaining
278 majority is produced by gluconeogenesis, primarily from lactate and glycerol (each about 25%).
279 For circulating lactate, about 20% is derived from intracellular glycogen breakdown and
280 subsequent glycolysis, in line with that measured by pulse-chase tracing of glycogen (TeSlaa et
281 al., 2021), while the remaining mostly comes from circulating glucose (60%) and glycerol (10%).
282 As glycerol is derived from TAG, this collectively shows that glycogen and TAG but not protein are
283 the major ultimate sources of circulating glucose (Wang et al., 2020). We further quantified such
284 ultimate contribution fraction from various storages to circulating nutrients (**Figure S4C**, see
285 derivation in **Suppl. Note 5**). Interestingly, while amino acids are typically released from the
286 protein as the principal source, alanine has its carbon origin roughly evenly from protein,
287 glycogen, and TAG.

288

289 **Sinks for Circulating Nutrients**

290 Together with the direct oxidation and storing fluxes calculated earlier (**Figure 3C**), the inter-
291 conversion fluxes of circulating nutrients constitute the direct sinks of circulating nutrients
292 (**Figure 4C**). This integrated view offers interesting insights. For example, though glutamine and
293 alanine, are known to be gluconeogenic, their direct conversion to lactate is more predominant
294 than to glucose. In addition, these amino acids are directly oxidized with higher fluxes than
295 otherwise relying on the lactate-genic pathway for energy supply.

296

297 **A Flux Model Incorporating All Quantified Fluxes for Circulating Nutrients**

298 A further inclusive combination of the production and consumption fluxes resulted in a
299 comprehensive metabolic flux model of circulating nutrients (**Figure 4D**). In addition to the
300 prominent oxidative fluxes for energy generation, this model vividly highlights two types of
301 cycling of the circulating nutrients. One type involves the cycling between the circulating
302 nutrients and the storages, and a second cycling exists between the circulating nutrients. These
303 cycles render a picture of vibrant carbon exchanges among nutrients in circulation and tissues.
304 Many of the futile cycles proceed at the cost of ATP. We estimated ATP wasted in the Cori cycle,
305 TAG-NEFA cycling, and protein turnover, the top three cycles with the highest carbon flux
306 (Methods). Together, these cycles wasted remarkably around 10% of the total ATP generated
307 (**Figure S4D**).

308

309 **Fluxes Are Generally Unperturbed in Diet-Induced Obese Mice**

310 To further demonstrate the utility of the systems-level flux modeling, we applied the framework
311 to two obese mouse models, high fat diet-induced obese mice (HFD), and leptin-deficient ob/ob
312 mice (**Figures 5-6, S5**). Unexpectedly, despite being 60% heavier than the wild-type control mice
313 on chow diet, the HFD mice showed generally moderate changes in f_{ox} and fluxes (**Figures 5A-**
314 **D**). The most striking change is the significantly increased production of circulating glycerol from
315 glucose. While it was elevated by 2-fold in ob/ob mice, it was more impressively activated by 4.5-
316 fold in the HFD group (**Figures 5B**, **S6, S7A**). The production of glycerol from glucose may be

317 derived from the recently discovered glycerol shunt pathway (Mugabo et al., 2016; Possik et al.,
318 2023), or from the spillover of the glycerol backbone in the very-low-density lipoprotein (VLDL)-
319 TAG during lipase hydrolysis, where the backbone is synthesized from blood glucose in the liver
320 (Jensen et al., 2001).
321
322 **Extensive Elevation of Metabolic Cycling in ob/ob Mice**
323 In contrast to the HFD mice, ob/ob mice showed major changes in energy metabolism. While f_{ox}
324 was moderately decreased for many nutrients, it was most prominently decreased by 2-fold in
325 circulating NEFAs (**Figures 5A**). This was accompanied by a 2-fold increase on average in the
326 NEFAs' circulatory turnover flux (equal to total consumption flux and total production flux)
327 (Turner et al., 2005), resulting in their unchanged oxidation flux, but a 2.3-fold elevation in the
328 recycling flux (**Figures 5B-D**). Intracellular reesterification nonetheless remained unchanged
329 (**Figure S8A**). The circulatory fluxes of both glucose and lactate were also increased by around 2-
330 fold (Turner et al., 2005), with production from different sources roughly proportionally scaled
331 up. This led to a 2.3-fold increase in the oxidation of the carbohydrate nutrients (coupled with
332 higher respiratory exchange ratio, **Figure S5D**), and over 2-fold increase in the fluxes of glucose
333 recycling to storage and Cori cycle. While the increased metabolic fluxes in ob/ob mice may be
334 attributed to a larger body mass, this effect can be statistically teased out using the generalized
335 linear model approach (Mina et al., 2018). Statistical adjustment for body weight suggests that
336 the augmented metabolic fluxes in ob/ob mice are more likely a result of metabolic rewiring
337 inherent to the phenotype (**Figure S7B**). In addition, the flux distinction retains even when the
338 ob/ob mice are compared to body-weight matched HFD mice (**Figure S7B**). Interestingly, as
339 gauged by the essential amino acid valine, the global protein oxidation and futile recycling
340 remains unchanged. All nutrients considered, the futile storing flux was 60% higher than their
341 oxidation flux. The total ATP wasted in the top 3 futile cycles, TAG-NEFA extracellular recycling,
342 Cori cycle and protein turnover, was 34% higher in ob/ob mice than the chow-fed control mice
343 (**Figure S8B**).
344
345 **DISCUSSION**

346 The present flux framework is a major advancement over our previous work (Hui et al., 2020),
347 where we systematically quantified the inter-converting fluxes between circulating nutrients
348 using isotope labeling data of serum metabolites. Here, by integrating $^{13}CO_2$ tracing to the
349 classic mass spectrometry-based isotope tracing framework, our framework further outputs the
350 oxidation, storage and releasing fluxes of circulating nutrients. Together with the inter-
351 converting fluxes, these fluxes form a full account of sources and sinks for circulating nutrients
352 at the organism level, resulting in a coherent flux model of energy metabolism. Analogous to a
353 map showing traffic along major highways in a city, our flux model captures the top fluxes in an
354 animal body, providing an overview of energy metabolism landscape for the animal. Such a flux
355 model for a disease state reveals unbiasedly the major alterations in energy metabolism for
356 that disease, setting the stage for further investigations.

357 Our flux model revealed extensive metabolic cycling in the fasted state, with higher total
358 flux than total oxidation flux. During fasting, the animal body is in a net catabolic state, with
359 nutrient storages such as glycogen, TAG, and proteins being actively broken down to replenish
360 circulating nutrients for oxidation into CO_2. Yet, recycling back into the storage pools is a
361 quantitatively more significant fate for circulating nutrients. What is the function of the extensive
362 cycling? One hypothesis is that it is to produce heat, to maintain or elevate body temperature
363 (Brownstein et al., 2022; Oeckl et al., 2022; She et al., 2007; Wolfe et al., 1987). We estimated
364 substantial energy used by these futile cycles, about 10% total ATP generated. Another probable
365 hypothesis is that metabolic cycling is to increase the sensitivity of metabolic regulation by
366 enhancing the response magnitude for changes in the stimulus (e.g., substrate
367 concentration)(Newsholme, 1978). We further revealed distinct partition between oxidation and
368 cycling fluxes for different circulating nutrients, e.g., about 80% of circulating glucose is burned,
369 while it is only ~40% for a fatty acid, and ~30% for an essential amino acid. The larger extent of
370 metabolic cycling in fatty acids and amino acids may thus reflect their relatively less hormonal
371 control than glucose. These and other hypotheses regarding the underlying principles of the
372 presence of extensive cycling flux and of distinct f_{ox} values across nutrients deserve further
373 investigations.

374 Our comprehensive flux results allow for comparison of fluxes between metabolic
375 processes and can expose flux mismatches and thus knowledge gaps. This way, we identified an
376 important gap in our understanding of the TAG-NEFA cycle, specifically regarding the sources of
377 glycerol backbone for resynthesis of TAG. The flux through the TAG-NEFA cycle constitutes the
378 major fraction of metabolic cycling, indicating active re-esterification of circulating NEFAs in
379 adipose tissues (Kalderon et al., 2000). Glucose is classically viewed as the main source for
380 glycerol backbone in TAG synthesis in adipose tissues (Sharma et al., 2024). However, even if all
381 the glucose storing flux is diverted to adipose tissues for producing glycerol backbone, it would
382 be insufficient to meet the demand (**Figure S8C**). Though lactate has been proposed as a supply
383 of the glycerol carbons in the adipose tissue via the glyceroneogenesis pathway (Hanson et al.,
384 2006), our data shows that circulating lactate has negligible flux fated to storages. Instead, our
385 quantification shows that circulating glycerol has significant flux to storage, numerically and
386 hypothetically fulfilling most of the needed glycerol backbone for TAG-resynthesis (**Figure S8C**).
387 However, on the other hand, adipose tissue lacks glycerol kinase, and cannot sequester
388 circulating glycerol directly. Therefore, the missing carbon source to synthesize TAG-glycerol
389 backbone remains an important topic to be further investigated.
390 The flux results of HFD and ob/ob obesity models demonstrated strikingly distinct energy
391 metabolism between them. Energy metabolic fluxes were mostly maintained in the HFD mice
392 while there was extensive elevation of cycling fluxes in the ob/ob mice. While body weight
393 differences can be a contributing factor, analysis of covariance (ANCOVA) with adjusted body
394 weight unveils that the flux differences are more likely a result of intrinsic distinctions between
395 phenotypes. Distinct fluxes in body weight-matched HFD and ob/ob group further supports this
396 viewpoint. It is possible that the HFD mice resemble the “healthy obesity” group in human
397 population, who are metabolically healthy despite being obese. On the other hand, the ob/ob
398 mice lie in a totally different part of the energy metabolism space, possibly mirroring their
399 departure from the state of metabolic health. Thus, instead of the commonplace view that ob/ob
400 mice are an “artificial” obesity model, HFD mice and ob/ob mice may model two states along the
401 progression of obesity.

402 The elevated glucose production and consumption fluxes in ob/ob mice inform on the
403 cause of hyperglycemia. In general, an increase of a metabolite pool could result from either a
404 blockage in the consumption reactions or an elevation in the production reactions. As production
405 and consumption balance each other in the new steady state, the flux through the pool can be
406 either reduced (in the consumption blockage case) or increased (in the production elevation case)
407 compared to the unperturbed state. By this argument, the increased flux through the glucose
408 pool in the ob/ob mice indicates elevated glucose production as the cause of hyperglycemia,
409 implicating liver insulin resistance instead of muscle insulin resistance as the driver of
410 hyperglycemia (Kraegen et al., 1991; Turner et al., 2013).
411
412 **Limitation**
413 The identities of nutrient storages were not explicitly studied in this work, but determined
414 based on literature knowledge. For example, triglycerides and proteins are storage for NEFAs and
415 amino acids, respectively. However, while it is commonly assumed that glycogen is the storage
416 for glucose, we recognize literature evidence pointing to other forms of tissue storages for
417 glucose, such as proteins (Shipley et al., 1967, 1970). Furthermore, as glucose is a substrate for
418 the glycerol backbone of tissue TAG, there is likely substantial flux from glucose to this form of
419 nutrient storage. A thorough investigation of the storages with new experimental designs would
420 be a critical future objective. In addition, our list of circulating nutrients did not include circulating
421 TAG; despite its larger pool size than NEFA, TAG has a small circulatory turnover flux (Gormsen
422 et al., 2006; Lambert et al., 2014; Sarac et al., 2012), and accounts for a minor fraction of total
423 lipid oxidation (Diraison and Beylot, 1998). As VLDL-TAG is mostly derived from circulating NEFA
424 and was labeled by ^{13}C-FA tracer during the time frame of our f_{ox} measurement (Parks and
425 Hellerstein, 2006; Parks et al., 1999), its oxidation and storage fluxes were mostly accounted for
426 in the NEFA fluxes, especially for lean mice. Future work is needed to explicitly delineate the NEFA
427 and TAG fluxes. Finally, our work focused on establishing the flux framework and for this purpose
428 only studied fasted male mice. Application of this framework to female animals and to other
429 physiological conditions such as feeding is of great importance.
430

ACKNOWLEDGEMENTS

The authors thank all current members and alumni of the Hui lab for their assistance and discussion in the research. This research was supported by the Paul G. Allen Family Foundation 0034665 (S.H.), the NIH R00DK117066 (S.H.), and the Sabri Ülker Center for Metabolic Research. Some figures were created with BioRender.com.

AUTHOR CONTRIBUTIONS

B.Y. designed and conducted the experiment, analyzed data, and wrote the manuscript. O.T. and W.D. performed the hyperinsulinemia clamp, ITT and GTT. Y.Y.K. performed the lipolysis enzymatic activity assay. K.I. supervised and assisted with the metabolic cage measurement. G.H. co-supervised the metabolic cage measurement and proposed critical revision to the manuscript. S.H. conceived and supervised the project, secured funding, and wrote the manuscript. All authors reviewed and contributed feedback to the manuscript.

DECLARATION OF INTERESTS

The authors declare no competing interests.

449 **STAR METHODS**

450 **KEY RESOURCES TABLE**

REAGENT or RESOURCE	SOURCE	IDENTIFIER
Chemicals, Peptides, and Recombinant Proteins		
D-glucose ($^{14}C_6$)	PerkinElmer	NEC042V250UC
D-glucose ($^{13}C_6$, 99%)	Cambridge Isotope Laboratories	CLM-1396
sodium L-lactate ($^{13}C_3$, 98%) 20% w/w in H_2O	Cambridge Isotope Laboratories	CLM-1579
L-alanine ($^{13}C_3$, 99%)	Cambridge Isotope Laboratories	CLM-2184-H
L-glutamine ($^{13}C_5$, 99%)	Cambridge Isotope Laboratories	CLM-1822-H
glycerol ($^{13}C_3$, 99%)	Cambridge Isotope Laboratories	CLM-1510
sodium D-3-hydroxybutyrate ($^{13}C_4$, 99%)	Cambridge Isotope Laboratories	CLM-3853
sodium acetate ($^{13}C_2$, 99%)	Cambridge Isotope Laboratories	CLM-440
sodium palmitate ($^{13}C_{16}$, 98%)	Cambridge Isotope Laboratories	CLM-6059
oleic acid, potassium salt ($^{13}C_{18}$, 98%)	Cambridge Isotope Laboratories	CLM-8856
linoleic acid, potassium salt ($^{13}C_{18}$, 98%)	Cambridge Isotope Laboratories	CLM-8835
L-valine ($^{13}C_5$, 99%)	Cambridge Isotope Laboratories	CLM-2249-H
bovine serum albumin, fatty acid free, ≥96%	Sigma-Aldrich	A6003
glycerokinase	Sigma-Aldrich	G6278
Ultra Sensitive Mouse Insulin ELISA Kit	Crystal Chem	90080
Experimental Models: Organisms/Strains		
Mouse: C57BL/6J	Jackson laboratory	000664
Mouse: ob/ob <HO>	Jackson laboratory	000632
Software and Algorithms		
El-MAVEN software	Elucidata https://docs.polly.elucidata.io/index.html	
RStudio	Posit https://posit.co/download/rstudio-desktop/	
AccuCor	Github: https://github.com/XiaoyangSu/AccuCor	
Biorender	Biorender https://www.biorender.com/	
Others		
chow diet	PicoLab Mouse Diet 20	5058
high fat diet	Research Diets	D12492i
XBridge BEH Amide XP column	Waters	176002889
Acquity UPLC BEH C18 column	Waters	186003719
catheter for mouse jugular vein	Instech Laboratories	C20PUMJV1301
catheter for mouse carotid artery	Instech Laboratories	C10PU-MCA1459
vascular access button, 1 channel	Instech Laboratories	VABM1B/25
vascular access button, 2 channels	Instech Laboratories	VABM2B/25R25
tether for 1 channel button	Instech Laboratories	VABM1T/25
tether for 2 channel button	Instech Laboratories	VABM2T/25
Buprenorphine base ER 0.5 mg/mL	Wedgewood	Rx # 7270862
Swivel	Instech Laboratories	375/25PS
counter balanced arm	Instech Laboratories	SMCLA
Blood collection Microvette	Starstedt Inc	16.440.100
Heparin sodium 5000 U/mL	McKesson Corp.	-

451

452

453 **RESOURCE AVAILABILITY**

454

455 **Lead Contact**

456 Additional information and requests for resources should be directed to the Lead Contact, Sheng
457 Hui (shui@hsph.harvard.edu).

458

459 **Materials AVAILABILITY**

460 No new reagents were generated in this study.

461

462 **Data and Code Availability**

463 Raw data and R scripts used for flux analysis is available on GitHub
464 (https://github.com/yuanboFaith/flux-model-energy-metabolism).

465

466 **EXPERIMENTAL MODEL AND SUBJECT DETAILS**

467 All mouse work followed protocols approved by the Institutional Animal Care and Use Committee
468 of Harvard Medical Area. The animals were housed on a normal light cycle (7 AM to 7 PM), and
469 were 12-24 weeks old when used in experiment. The wild type C57BL/6J and ob/ob mice were
470 fed with standard chow (PicoLab Mouse Diet 5058). For diet-induced obese mice, C57BL/6J mice
471 were fed with high fat diet (Research Diets D12492i, 60%kcal from fat) starting from the 3 weeks
472 of age for 3-4 months before experiment. For *in vivo* tracer infusion, a jugular vein catheter (JVC)
473 was inserted into the right jugular vein, under aseptic conditions and with anesthesia using
474 isoflurane. The JVC was tunneled subcutaneously to the back of the interscapular area, and
475 connected to a single-channel vascular access button (VAB). For arterial blood collection, in
476 addition to jugular catheterization, a carotid artery catheter (CAC) was implanted into the left
477 carotid artery. Both the JVC and CAC were subcutaneously tunneled to the interscapular region,
478 and connected to a double-channel VAB. The catheter patency was maintained by sealing with
479 lock solution composed of 50% glycerol in saline, with 200 U heparin/mL. After surgery, 50 µL of
480 0.5 mg/mL analgesic buprenorphine (extended release) per 25 g body weight was
481 subcutaneously injected to the right flank. The animal was allowed to recover from surgery for
482 at least five days before use in experiment.

483

484 **METHOD DETAILS**

485

486 **$^{13}CO_2$ Measurement**

487 ^{13}C-labeled tracer compounds were prepared in sterile saline. Fatty acids were complexed with
488 bovine serum albumin in a molar ratio of 6:1. For $^{13}CO_2$ measurements after tracer bolus injection,
489 the mouse was transferred to a new cage without food at 9:00 AM. After 4 hours of fasting, the
490 animal was gently warmed by a heat lamp to dilate the tail vein. Under light isoflurane anesthesia,
491 the mouse was administered with 200 µL ^{13}C-tracer solution via the tail vein. The animal was then
492 immediately transferred to a cage in the metabolic cage system, which was equipped with a
493 stable isotope gas analyzer (Promethion, Sable Systems International, NV). Expired $^{13}CO_2$ and
494 metabolic cage parameters including air flow rate, oxygen, and CO_2 were monitored for another
495 6 hours without food access.

496 $^{13}CO_2$ measurement with tracer infusion required catharized mice and followed the same
497 protocol described in the tracer infusion section below, except that the infusion lasted for 3-4
498 hours, with a reduced tracer concentration. The tracer concentration and infusion rates can be
499 found in **Table S1**. $^{13}CO_2$ data and metabolic cage parameters including air flow rate, oxygen, and
500 CO_2 were continuously collected for the entire period of tracer infusion.

501

502 **Infusion of Isotope Tracers**

503 On the day of tracer infusion, the mouse was transferred to a new cage without food at 9 AM,
504 and fasted for 4 hours before infusion. Right before the start of infusion, the lock solution was
505 drawn and removed from the catheter, and the catheter was flushed with 50 µL saline. The VAB
506 was then connected to the infusion tether, which was in turn connected with a swivel on a
507 counter-balance arm. This allowed the mouse to move freely around in the cage. The infusion of
508 U-^{13}C-tracer at a small non-perturbing dose started at 2 PM, and lasted for 30 min for fatty acids
509 and 2.5-3 h for all other tracers. The tracer concentration and infusion rates can be found in **Table**
510 **S1**. At the end of infusion, 40 µL blood was collected by tail snip. For infusion of ^{13}C-lactate,
511 alanine, and glutamine, given their significant labeling difference in the arterial and venous blood
512 (**Table S2**)(Lee et al., 2023), 40 µL arterial blood was sampled from the carotid artery via the pre-

513 implanted catheter, and used for analysis. The blood was collected into a Microvette tube with
514 clotting activator, and was kept on ice during collection. After infusion, the catheter was flushed
515 with 50 µL saline, and then sealed with 10 ~ 20 µL lock solution. The blood was centrifuged at
516 5,000 ×g for 10 min. 4 µL serum was aliquoted in separate tubes, and stored at -80°C.
517
518 **Hyperinsulinemia Clamp**
519 BL/6J mouse (26.5 ± 1.8 g) was transferred to a new cage without food at 9 AM. After fasting for
520 4 hours, blood was collected via tail snip for basal glycemia and insulin measurement. A mixture
521 of U-^{13}C-glucose (150 mM), unlabeled glucose (2361 mM) and insulin (66.6 mU/mL) was infused
522 at 3.3 µL/min/mouse for 2.5 h, and blood was collected for serum glucose labeling and insulin
523 measurement. Then U-^{13}C palmitate (10.68 mM) was infused at 6 µL/min/animal for another 30
524 min (delivered by a second pump), simultaneously with the glucose and insulin infusion. Blood
525 was collected at the end for serum glucose and palmitate labeling and insulin measurement.
526 Insulin was measured by ELISA Kit following the vendor's protocol.
527
528 **Serum Sample Preparation for LC-MS Analysis**
529 4 µL serum was mixed with 60 µL -20°C methanol: acetonitrile: water at 40: 40: 20. The sample
530 was vigorously vortexed, and centrifuged at 4°C at 13,000 g for 10 min. 30 µL supernatant was
531 transferred to the HPLC vial from which 5 µL was injected to the LC-MS.
532 Serum glycerol was first enzymatically derivatized into glycerol-3-phosphate before LC-MS
533 analysis. 4 µL serum was mixed with 90 µL freshly made enzyme solution containing 2 U/mL
534 glycerol kinase, 25 mM Tris-HCl (pH 8.0), 50 mM sodium chloride, 10 mM magnesium chloride,
535 and 1.5 mM ATP, and incubated at room temperature for 15 min. The reaction was stopped by
536 the addition of 400 µL methanol. The sample was vortexed, and centrifuged at 16,000 g for 10
537 min. The supernatant was transferred to a new tube, and dried using SpeedVac at 45 °C for 90
538 min. 60 µL of methanol: acetonitrile: water at 40: 40: 20 was added to the residue, vortexed, and
539 centrifuged at 16,000 g for 10 min. 30 µL supernatant was transferred to the HPLC vial, from
540 which 5 µL was injected to the LC-MS.
541

542 **LC-MS Analysis**

543 Chromatographic separation was achieved using XBridge BEH Amide XP Column (2.5 µm, 2.1 mm
544 × 150 mm) with guard column (2.5 µm, 2.1 mm × 5 mm) (Waters, Milford, MA). The mobile phase
545 A was water: acetonitrile 95:5, and mobile phase B was water: acetonitrile 20:80, with both
546 phases containing 10 mM ammonium acetate and 10 mM ammonium hydroxide. The elution
547 linear gradient was: 0 ~ 3 min, 100% B; 3.2 ~ 6.2 min, 90% B; 6.5. ~ 10.5 min, 80% B; 10.7 ~ 13.5
548 min, 70% B; 13.7 ~ 16 min, 45% B; and 16.5 ~ 22 min, 100% B, with flow rate of 0.3 mL/min. The
549 autosampler was at 4˚C. The injection volume was 5 µL. Needle wash was applied between
550 samples using methanol: acetonitrile: water at 40: 40: 20. The mass spectrometer used was Q
551 Exactive HF (Thermo Fisher Scientific, San Jose, CA), and scanned from 70 to 1000 *m/z* with
552 switching polarity. The resolution was 120,000. Metabolites were identified based on accurate
553 mass and retention time using an in-house library. ^{13}C-Natural abundance correction was
554 performed in R using package AccuCor (Su et al., 2017).

555

556 **^{14}C-glucose administration and carcass analysis**

557 The mouse was fasted from 9 AM to 12 PM, and then 12 nCi $^{14}C_6$-glucose in 200 µL saline was
558 administered via the tail vein. After 6 h, the animal was sacrificed, and the hair was shaved off.
559 The carcass was transferred into an Erlenmeyer flask containing 70 mL 1.7 M KOH, and
560 microwaved to simmer. The flask was incubated at 90 C° for 3 h for complete carcass digestion.
561 After having cooled down to room temperature, the total liquid volume was measured, and 2 mL
562 15% antifoam B emulsion (Sigma A5757) and 1 mL Tween 80 (Sigma P4780) was added to the
563 digest. Under magnetic stirring, 0.4 mL of the digest was sampled and transferred to a scintillation
564 vial. A mix of 150 µL 2 M acetic acid, 200 µL 50% H_2O_2, and 50 µL 15% antifoam B was added to
565 the vial, followed by incubation at 70C° for 20 min to decolorize the mixture. The vial was then
566 added with 200 µL of 12 M acetic acid and 5 mL Ecolume scintillation liquid (MP Biomedicals,
567 0188247001) and vigorously vortexed. ^{14}C radioactivity in the vial was measured using a HIDEX
568 300 SL liquid scintillation counter (Turku, Finland).

569

570 **QUANTIFICATION AND STATISTICAL ANALYSIS**

571 **Calculation of the Fraction of Oxidation (f_{ox}) of a Circulating Nutrient**

572 The f_{ox} of a circulating nutrient was calculated as the fraction of ^{13}C atoms in the exhaled CO_2
573 among the total ^{13}C atoms in the administered tracer. For a mouse in a metabolic cage system
574 administered with a ^{13}C tracer, the production flux of tracer-derived $^{13}CO_2$ from the animal J
575 (μmol/min) was calculated as

$$J = \frac{Q}{22.4(1 - E_{NA})} \cdot [\, C_{out}(E_{out} - E_{NA}) - C_{in}(E_{in} - E_{NA})] \cdot 10^{-3} \qquad \text{(Equation 8)}$$

576 where Q is the air flow rate through the cage, C_{in} and C_{out} are the CO_2 concentration measured
577 in the air inflow and outflow respectively, E_{in} and E_{out} are the $^{13}CO_2$ enrichment measured in
578 the air inflow and outflow, respectively, and E_{NA} is the ^{13}C natural abundance of the unlabeled
579 nutrients in the mouse body. E_{NA} was calculated using Eq. (8) from measured CO_2 concentration
580 and enrichment data for a non-infused control mouse group and a production flux of tracer-
581 derived $^{13}CO_2$ as zero ($J = 0$). For an animal under the infusion at the rate of I (μmol ^{13}C-
582 atoms/min), the f_{ox} was then calculated as

$$f_{ox} = \frac{J}{I} \qquad \text{(Equation 9)}$$

583 For animal receiving the tracer as a single bolus at dosage of B (μmol ^{13}C-atoms), the fraction of
584 oxidation f_{ox} was calculated as

$$f_{ox} = \frac{1}{B} \int_{t=0}^{\infty} J \, dt \qquad \text{(Equation 10)}$$

585 with integration from the time of injection to the end of measurement when CO_2 enrichment
586 reached basal level. Details of the derivations are in **Suppl. Note 1**.

587

588 **Calculation of Fluxes to Oxidation (J_{OX}) and Storages (J_S) from a Circulating Nutrient**

589 The J_{ox} and J_S were calculated using Eqs. (1) and (2) in the main text, respectively. The labeling
590 L used here and throughout the text was the carbon-atom labeling fraction of the nutrient. It is
591 calculated as

$$L = \frac{1}{N}\sum_{i=1}^{N} i \cdot L_{M+i} \qquad \text{(Equation 11)}$$

where N is the number of carbon atoms in a molecule, and L_{M+i} is the fraction of isotopologue containing i number of ^{13}C atoms among all isotopologues of the molecule. Details of the derivations are in **Suppl. Note 2**.

Calculation of the *Direct* Fluxes to Oxidation (O) and Storage (S) from Circulating Nutrients

The direct oxidation fluxes O_j of N circulating nutrients were calculated with Eq. (5) in the main text. The direct storing fluxes S_j of the circulating nutrients were calculated with

$$\boldsymbol{A} \cdot \begin{bmatrix} S_1 \\ S_2 \\ \vdots \\ S_N \end{bmatrix} = \begin{bmatrix} I_1(1 - f_{ox_1}) \\ I_2(1 - f_{ox_2}) \\ \vdots \\ I_N(1 - f_{ox_N}) \end{bmatrix} \qquad \text{(Equation 12)}$$

where I_j and f_{ox_j} are the infusion rate and the fraction of oxidation of nutrient j, respectively. The matrix $\boldsymbol{A}$ is defined as

$$\boldsymbol{A} = \begin{bmatrix} \frac{L_1^1}{1 - L_1^1} & \frac{L_2^1}{1 - L_2^1} & \cdots & \frac{L_N^1}{1 - L_N^1} \\ \frac{L_1^2}{1 - L_1^2} & \frac{L_2^2}{1 - L_2^2} & \cdots & \frac{L_N^2}{1 - L_N^2} \\ \vdots & \vdots & \ddots & \vdots \\ \frac{L_1^N}{1 - L_1^N} & \frac{L_2^N}{1 - L_2^N} & \cdots & \frac{L_N^N}{1 - L_N^N} \end{bmatrix} \qquad \text{(Equation 13)}$$

where L_j^k is the labeling of nutrient j under the infusion of ^{13}C-labeled nutrient k. The unknowns O_j and S_j were solved with the method of least squares, subjected to $O_j \geq 0$ and $S_j \geq 0$, using R package LimSolve, and function lsei (least squares with equalities and inequalities) (Soetaert, 2009). The error was approximated with Monte Carlo simulation. For Eqs. (5) and (12), respectively, we ran the matrix optimization 100 times. In each optimization, for each L_j^k and f_{ox_j} value, a random value was drawn from a normal distribution, with mean and standard deviation (SD) being the mean and standard error of the mean (SEM) of these measured quantities. The SD

608 of the 100 simulated $\boldsymbol{O}$ and $\boldsymbol{S}$ vectors were taken as the associated SEM, respectively. More
609 details of the calculation can be found in **Suppl. Note 3**.
610
611 **Calculation of the Storage Releasing Flux ($\boldsymbol{F_s}$) to a Circulating Nutrient, and Conversion Fluxes**
612 **($\boldsymbol{F_j}$) between Circulating Nutrients**
613 To calculate the storage-releasing flux F_s and the converting fluxes F_j from n different circulating
614 nutrients to a target nutrient (TN) of interest, ^{13}C-labeled TN and the n source nutrients were
615 infused individually to the animals. Each infusion generates an Eq. (7), with L_{TN} in replace of L_{glu}.
616 Integrating all $n+1$ equations gives the linear system

$$\boldsymbol{B} \cdot \begin{bmatrix} F_1 \\ F_2 \\ \vdots \\ F_n \\ F_s \end{bmatrix} = \begin{bmatrix} I(1-L_{TN}) \\ 0 \\ \vdots \\ 0 \\ 0 \end{bmatrix} \qquad \text{(Equation 14)}$$

617 with

$$\boldsymbol{B} = \begin{bmatrix} \frac{L_*^* - L_1^*}{1-L_1^*} & \frac{L_*^* - L_2^*}{1-L_2^*} & \cdots & \frac{L_*^* - L_n^*}{1-L_n^*} & \frac{L_*^* - L_s^*}{1-L_s^*} \\ \frac{L_*^1 - L_1^1}{1-L_1^1} & \frac{L_*^1 - L_2^1}{1-L_2^1} & \cdots & \frac{L_*^1 - L_n^1}{1-L_n^1} & \frac{L_*^1 - L_s^1}{1-L_s^1} \\ \vdots & \vdots & \ddots & \vdots & \vdots \\ \frac{L_*^n - L_1^n}{1-L_1^n} & \frac{L_*^n - L_2^n}{1-L_2^n} & \cdots & \frac{L_*^n - L_n^n}{1-L_n^n} & \frac{L_*^n - L_s^n}{1-L_s^n} \end{bmatrix} \qquad \text{(Equation 15)}$$

618 where $L_s^k = 0$. Asterisks are used in replace of *TN* for notation clarity. The matrix optimization
619 and error estimation were performed as above. More details of the calculation can be found in
620 **Suppl. Note 4**.

621

622 **Estimation of Energy Wasted in Futile Cycles**

623 The ATP flux that is wasted in the major futile cycles was estimated using the following
624 parameters: 4 ATP molecules wasted per cycling of one glucose molecule in the Cori cycle, 9-11
625 ATP molecules used in the resynthesis of each TAG molecule in the TAG-NEFA cycling, and 4 ATP

626 molecules used for synthesis of each peptide bond (Bender, 2012). The total flux of ATP
627 generation was calculated based on the direct carbon oxidation flux of circulating nutrients,
628 where the ATP yield is 5.3 per carbohydrate carbon, 6.5 per fatty acid carbon, 5.5 per ketone
629 body carbon, and 5 per amino acid carbon (Bender, 2012). More details of the calculation are in
630 **Suppl. Note 6**.

631

632 **REFERENCES**

633 Antoniewicz, M.R. (2018). A guide to 13C metabolic flux analysis for the cancer biologist. Exp. Mol. Med. *50*.
634 https://doi.org/10.1038/s12276-018-0060-y.

635 Befroy, D.E., Perry, R.J., Jain, N., Dufour, S., Cline, G.W., Trimmer, J.K., Brosnan, J., Rothman, D.L., Petersen,
636 K.F., and Shulman, G.I. (2014). Direct assessment of hepatic mitochondrial oxidative and anaplerotic fluxes in humans
637 using dynamic 13 C magnetic resonance spectroscopy. Nat. Med. *20*, 98–102. https://doi.org/10.1038/nm.3415.

638 Bender, D.A. (2012). The metabolism of "surplus" amino acids. Br. J. Nutr. *108*, 7–10.
639 https://doi.org/10.1017/S0007114512002292.

640 Brownstein, A.J., Veliova, M., Acin-Perez, R., Liesa, M., and Shirihai, O.S. (2022). ATP-consuming futile cycles
641 as energy dissipating mechanisms to counteract obesity. Rev. Endocr. Metab. Disord. *23*, 121–131.
642 https://doi.org/10.1007/s11154-021-09690-w.

643 Campbell, P.J., Carlson, M.G., Hill, J.O., and Nurjhan, N. (1992). Regulation of free fatty acid metabolism by
644 insulin in humans: Role of lipolysis and reesterification. Am. J. Physiol. - Endocrinol. Metab. *263*.
645 https://doi.org/10.1152/ajpendo.1992.263.6.e1063.

646 Cappel, D.A., Deja, S., Duarte, J.A.G., Kucejova, B., Iñigo, M., Fletcher, J.A., Fu, X., Berglund, E.D., Liu, T.,
647 Elmquist, J.K., et al. (2019). Pyruvate-Carboxylase-Mediated Anaplerosis Promotes Antioxidant Capacity by
648 Sustaining TCA Cycle and Redox Metabolism in Liver. Cell Metab. *29*, 1291-1305.e8.
649 https://doi.org/10.1016/j.cmet.2019.03.014.

650 Coppack, S.W., Persson, M., Judd, R.L., and Miles, J.M. (1999). Glycerol and nonesterified fatty acid
651 metabolism in human muscle and adipose tissue in vivo. Am. J. Physiol. - Endocrinol. Metab. *276*, 233–240.
652 https://doi.org/10.1152/ajpendo.1999.276.2.e233.

653 Cori, C.F. (1931). Mammalian Carbohydrate Metabolism. Physiol. Rev. *11*, 143–275.
654 https://doi.org/10.1152/physrev.1931.11.2.143.

655 Elia, M., Fuller, N.J., and Murgatroyd, P.R. (1992). Measurement of bicarbonate turnover in humans:
656 Applicability to estimation of energy expenditure. Am. J. Physiol. - Endocrinol. Metab. *263*.
657 https://doi.org/10.1152/ajpendo.1992.263.4.e676.

658 Fearon, K.C.H., Hansell, D.T., Preston, T., Plumb, J.A., Davies, J., Shapiro, D., Shenkin, A., Calman, K.C., and
659 Burns, H.J.G. (1988). Influence of Whole Body Protein Turnover Rate on Resting Energy Expenditure in Patients with
660 Cancer. Cancer Res. *48*, 2590–2595. .

661 Fernández-García, J., Altea-Manzano, P., Pranzini, E., and Fendt, S.M. (2020). Stable Isotopes for Tracing
662 Mammalian-Cell Metabolism In Vivo. Trends Biochem. Sci. *45*, 185–201. https://doi.org/10.1016/j.tibs.2019.12.002.

663 Gorissen, S.H.M., and Phillips, S.M. (2018). Branched-chain amino acids (leucine, isoleucine, and valine) and
664 skeletal muscle (Elsevier Inc.).

665 Gormsen, L.C., Jensen, M.D., Schmitz, O., Møller, N., Christiansen, J.S., and Nielsen, S. (2006). Energy
666 expenditure, insulin, and VLDL-triglyceride production in humans. J. Lipid Res. *47*, 2325–2332.
667 https://doi.org/10.1194/jlr.M600175-JLR200.

668 Hanson, R.W., Ballard, F.J., and Reshef, L. (2006). Glyceroneogenesis, the pathway that almost wasn't.
669 Biochem. Mol. Biol. Educ. *34*, 317–323. https://doi.org/10.1002/bmb.2006.494034052637.

670 Hasenour, C.M., Rahim, M., and Young, J.D. (2020). In Vivo Estimates of Liver Metabolic Flux Assessed by 13C-
671 Propionate and 13C-Lactate Are Impacted by Tracer Recycling and Equilibrium Assumptions. Cell Rep. *32*.
672 https://doi.org/10.1016/j.celrep.2020.107986.

673 Hui, S., Ghergurovich, J.M., Morscher, R.J., Jang, C., Teng, X., Lu, W., Esparza, L.A., Reya, T., Zhan, L., Yanxiang
674 Guo, J., et al. (2017). Glucose feeds the TCA cycle via circulating lactate. Nature *551*, 115–118.
675 https://doi.org/10.1038/nature24057.

676 Hui, S., Cowan, A.J., Zeng, X., Yang, L., TeSlaa, T., Li, X., Bartman, C., Zhang, Z., Jang, C., Wang, L., et al. (2020).
677 Quantitative Fluxomics of Circulating Metabolites. Cell Metab. *32*, 676-688.e4.
678 https://doi.org/10.1016/j.cmet.2020.07.013.

679 Jensen, M.D., Chandramouli, V., Schumann, W.C., Ekberg, K., Previs, S.F., Gupta, S., and Landau, B.R. (2001).
680 Sources of blood glycerol during fasting. Am. J. Physiol. - Endocrinol. Metab. *281*, 998–1004.
681 https://doi.org/10.1152/ajpendo.2001.281.5.e998.

682 Kalderon, B., Mayorek, N., Berry, E., Zevit, N., and Bar-Tana, J. (2000). Fatty acid cycling in the fasting rat. Am.
683 J. Physiol. - Endocrinol. Metab. *279*, 221–227. https://doi.org/10.1152/ajpendo.2000.279.1.e221.

684 Keller, U., Sonnenberg, G.E., and Stauffacher, W. (1981). Validation of a tracer technique to determine
685 nonsteady-state ketone body turnover rates in man. Am. J. Physiol. - Endocrinol. Metab. *3*.
686 https://doi.org/10.1152/ajpendo.1981.240.3.e253.

687 Kleberg, K., Nielsen, L.L., Stuhr-Hansen, N., Nielsen, J., and Hansen, H.S. (2014). Evaluation of the immediate
688 vascular stability of lipoprotein lipase-generated 2-monoacylglycerol in mice. BioFactors *40*, 596–602.
689 https://doi.org/10.1002/biof.1189.

690 Kraegen, E.W., Clark, P.W., Jenkins, A.B., Daley, E.A., Chisholm, D.J., and Storlien, L.H. (1991). Development
691 of muscle insulin resistance after liver insulin resistance in high-fat-fed rats. Diabetes *40*, 1397–1403.
692 https://doi.org/10.2337/diab.40.11.1397.

693 Lambert, J.E., Ramos-Roman, M.A., Browning, J.D., and Parks, E.J. (2014). Increased de novo lipogenesis is a
694 distinct characteristic of individuals with nonalcoholic fatty liver disease. Gastroenterology *146*, 726–735.

695 https://doi.org/10.1053/j.gastro.2013.11.049.

696 Lee, W.D., Liang, L., AbuSalim, J., Jankowski, C.S.R., Samarah, L.Z., Neinast, M.D., and Rabinowitz, J.D. (2023).
697 Impact of acute stress on murine metabolomics and metabolic flux. Proc. Natl. Acad. Sci. *120*, 2017.
698 https://doi.org/10.1073/pnas.2301215120.

699 Liss, K.H.H., Lutkewitte, A.J., Pietka, T., Finck, B.N., Franczyk, M., Yoshino, J., Klein, S., and Hall, A.M. (2018).
700 Metabolic importance of adipose tissue monoacylglycerol acyltransferase 1 in mice and humans. J. Lipid Res. *59*,
701 1630–1639. https://doi.org/10.1194/jlr.M084947.

702 Matthews, D.E., Motil, K.J., and Rorhrbaugh, D.K. (1980). Measurement of leucine metabolism in man from a
703 primed, continuous infusion of L-[1-13C]leucine. Am. J. Physiol. - Endocrinol. Metab. *1*.
704 https://doi.org/10.1152/ajpendo.1980.238.5.e473.

705 McCue, M.D., and Welch, K.C. (2016). 13C-Breath testing in animals: theory, applications, and future
706 directions. J. Comp. Physiol. B Biochem. Syst. Environ. Physiol. *186*, 265–285. https://doi.org/10.1007/s00360-015-
707 0950-4.

708 Metallo, C.M. (2015). Metabolic analysis using stable isotopes (Waltham, MA: Academic Press).

709 Mina, A.I., LeClair, R.A., LeClair, K.B., Cohen, D.E., Lantier, L., and Banks, A.S. (2018). CalR: A Web-Based
710 Analysis Tool for Indirect Calorimetry Experiments. Cell Metab. *28*, 656-666.e1.
711 https://doi.org/10.1016/j.cmet.2018.06.019.

712 Mugabo, Y., Zhao, S., Seifried, A., Gezzar, S., Al-Mass, A., Zhang, D., Lamontagne, J., Attane, C., Poursharifi, P.,
713 Iglesias, J., et al. (2016). Identification of a mammalian glycerol-3-phosphate phosphatase: Role in metabolism and
714 signaling in pancreatic β-cells and hepatocytes. Proc. Natl. Acad. Sci. U. S. A. *113*, E430–E439.
715 https://doi.org/10.1073/pnas.1514375113.

716 Newsholme, E.A. (1978). Substrate cycles: their metabolic, energetic and thermic consequences in man.
717 Biochem. Soc. Symp. 183–205. .

718 Nye, C., Kim, J., Kalhan, S.C., and Hanson, R.W. (2008). Reassessing triglyceride synthesis in adipose tissue.
719 Trends Endocrinol. Metab. *19*, 356–361. https://doi.org/10.1016/j.tem.2008.08.003.

720 Oeckl, J., Janovska, P., Adamcova, K., Bardova, K., Brunner, S., Dieckmann, S., Ecker, J., Fromme, T., Funda, J.,
721 Gantert, T., et al. (2022). Loss of UCP1 function augments recruitment of futile lipid cycling for thermogenesis in
722 murine brown fat. Mol. Metab. *61*, 101499. https://doi.org/10.1016/j.molmet.2022.101499.

723 Parks, E.J., and Hellerstein, M.K. (2006). Recent advances in liver triacylglycerol and fatty acid metabolism
724 using stable isotope labeling techniques. J. Lipid Res. *47*, 1651–1660. https://doi.org/10.1194/jlr.R600018-JLR200.

725 Parks, E.J., Krauss, R.M., Christiansen, M.P., Neese, R.A., and Hellerstein, M.K. (1999). Effects of a low-fat,

726 high-carbohydrate diet on VLDL-triglyceride assembly, production, and clearance. J. Clin. Invest. *104*, 1087–1096.
727 https://doi.org/10.1172/JCI6572.

728 Possik, E., Klein, L.L., Sanjab, P., Zhu, R., Côté, L., Bai, Y., Zhang, D., Sun, H., Al-Mass, A., Oppong, A., et al.
729 (2023). Glycerol 3-phosphate phosphatase/PGPH-2 counters metabolic stress and promotes healthy aging via a
730 glycogen sensing-AMPK-HLH-30-autophagy axis in C. elegans. Nat. Commun. *14*. https://doi.org/10.1038/s41467-
731 023-40857-y.

732 Del Prato, S., Bonadonna, R.C., Bonora, E., Gulli, G., Solini, A., Shank, M., and DeFronzo, R.A. (1993).
733 Characterization of cellular defects of insulin action in type 2 (non-insulin-dependent) diabetes mellitus. J. Clin. Invest.
734 *91*, 484–494. https://doi.org/10.1172/JCI116226.

735 Randle, P.J., Garland, P.B., Hales, C.N., and Newsholme, E.A. (1963). the Glucose Fatty-Acid Cycle Its Role in
736 Insulin Sensitivity and the Metabolic Disturbances of Diabetes Mellitus. Lancet *281*, 785–789.
737 https://doi.org/10.1016/S0140-6736(63)91500-9.

738 Reichard, G.A., Moury, N.F., Hochella, N.J., Patterson, A.L., and Weinhouse, S. (1963). Quantitative Estimation
739 of the Cori Cycle in the Human. J. Biol. Chem. *238*, 495–501. https://doi.org/10.1016/s0021-9258(18)81288-1.

740 Reshef, L., Olswang, Y., Cassuto, H., Blum, B., Croniger, C.M., Kalhan, S.C., Tilghman, S.M., and Hanson, R.W.
741 (2003). Glyceroneogenesis and the triglyceride/fatty acid cycle. J. Biol. Chem. *278*, 30413–30416.
742 https://doi.org/10.1074/jbc.R300017200.

743 Sarac, I., Backhouse, K., Shojaee-Moradie, F., Stolinski, M., Robertson, M.D., Bell, J.D., Thomas, E.L., Hovorka,
744 R., Wright, J., and Umpleby, A.M. (2012). Gender differences in VLDL1 and VLDL2 triglyceride kinetics and fatty acid
745 kinetics in obese postmenopausal women and obese men. J. Clin. Endocrinol. Metab. *97*, 2475–2481.
746 https://doi.org/10.1210/jc.2011-3248.

747 Scow, R.O., and Blanchette-Mackie, E.J. (1991). Transport of fatty acids and monoacylglycerols in white and
748 brown adipose tissues. Brain Res. Bull. *27*, 487–491. https://doi.org/10.1016/0361-9230(91)90147-C.

749 Sharma, A.K., Khandelwal, R., and Wolfrum, C. (2024). Futile lipid cycling: from biochemistry to physiology.
750 Nat. Metab. https://doi.org/10.1038/s42255-024-01003-0.

751 She, P., Reid, T.M., Bronson, S.K., Vary, T.C., Hajnal, A., Lynch, C.J., and Hutson, S.M. (2007). Disruption of
752 BCATm in Mice Leads to Increased Energy Expenditure Associated with the Activation of a Futile Protein Turnover
753 Cycle. Cell Metab. *6*, 181–194. https://doi.org/10.1016/j.cmet.2007.08.003.

754 Shi, Y., and Cheng, D. (2009). Beyond triglyceride synthesis: The dynamic functional roles of MGAT and DGAT
755 enzymes in energy metabolism. Am. J. Physiol. - Endocrinol. Metab. *297*, 10–18.
756 https://doi.org/10.1152/ajpendo.90949.2008.

757 Shipley, R.A., Chudzik, E.B., Gibbons, A.P., Jongedyk, K., and Brummond, D.O. (1967). Rate of glucose

758 transformation in the rat by whole-body analysis after blucose-14-C. Am. J. Physiol. *213*, 1149–1158.
759 https://doi.org/10.1152/ajplegacy.1967.213.5.1149.

760 Shipley, R.A., Chudzik, E.B., and Gibbons, A.P. (1970). Rate of disposal of glucose carbon to CO2, fat, protein,
761 and glycogen in the diabetic rat. Am. J. Physiol. *219*, 364–373. https://doi.org/10.1152/ajplegacy.1970.219.2.364.

762 Soetaert, K. (2009). Package limSolve, solving linear inverse models in R.

763 Su, X., Lu, W., and Rabinowitz, J.D. (2017). Metabolite Spectral Accuracy on Orbitraps. Anal. Chem *89*, 11.
764 https://doi.org/10.1021/acs.analchem.7b00396.

765 TeSlaa, T., Bartman, C.R., Jankowski, C.S.R., Zhang, Z., Xu, X., Xing, X., Wang, L., Lu, W., Hui, S., and Rabinowitz,
766 J.D. (2021). The Source of Glycolytic Intermediates in Mammalian Tissues. Cell Metab. *33*, 367-378.e5.
767 https://doi.org/10.1016/j.cmet.2020.12.020.

768 Tolbert, B.M., Kirk, M., and Baker, E.M. (1956). Continuous 14CO2 and CO2 Excretion Studies in Experimental
769 Animals. Am. J. Physiol. Content *185*, 269–274. https://doi.org/10.1152/ajplegacy.1956.185.2.269.

770 Turner, N., Kowalski, G.M., Leslie, S.J., Risis, S., Yang, C., Lee-Young, R.S., Babb, J.R., Meikle, P.J., Lancaster,
771 G.I., Henstridge, D.C., et al. (2013). Distinct patterns of tissue-specific lipid accumulation during the induction of
772 insulin resistance in mice by high-fat feeding. Diabetologia *56*, 1638–1648. https://doi.org/10.1007/s00125-013-
773 2913-1.

774 Turner, S.M., Linfoot, P.A., Neese, R.A., and Hellerstein, M.K. (2005). Sources of plasma glucose and liver
775 glycogen in fasted ob/ob mice. Acta Diabetol. *42*, 187–193. https://doi.org/10.1007/s00592-005-0201-3.

776 Wang, Y., Kwon, H., Su, X., and Wondisford, F.E. (2020). Glycerol not lactate is the major net carbon source
777 for gluconeogenesis in mice during both short and prolonged fasting. Mol. Metab. *31*, 36–44.
778 https://doi.org/10.1016/j.molmet.2019.11.005.

779 Wolfe, R.R., Herndon, D.N., Jahoor, F., Miyoshi, H., and Wolfe, M. (1987). Effect of Severe Burn Injury on
780 Substrate Cycling by Glucose and Fatty Acids. N. Engl. J. Med. *317*, 403–408.
781 https://doi.org/10.1056/NEJM198708133170702.

782

783

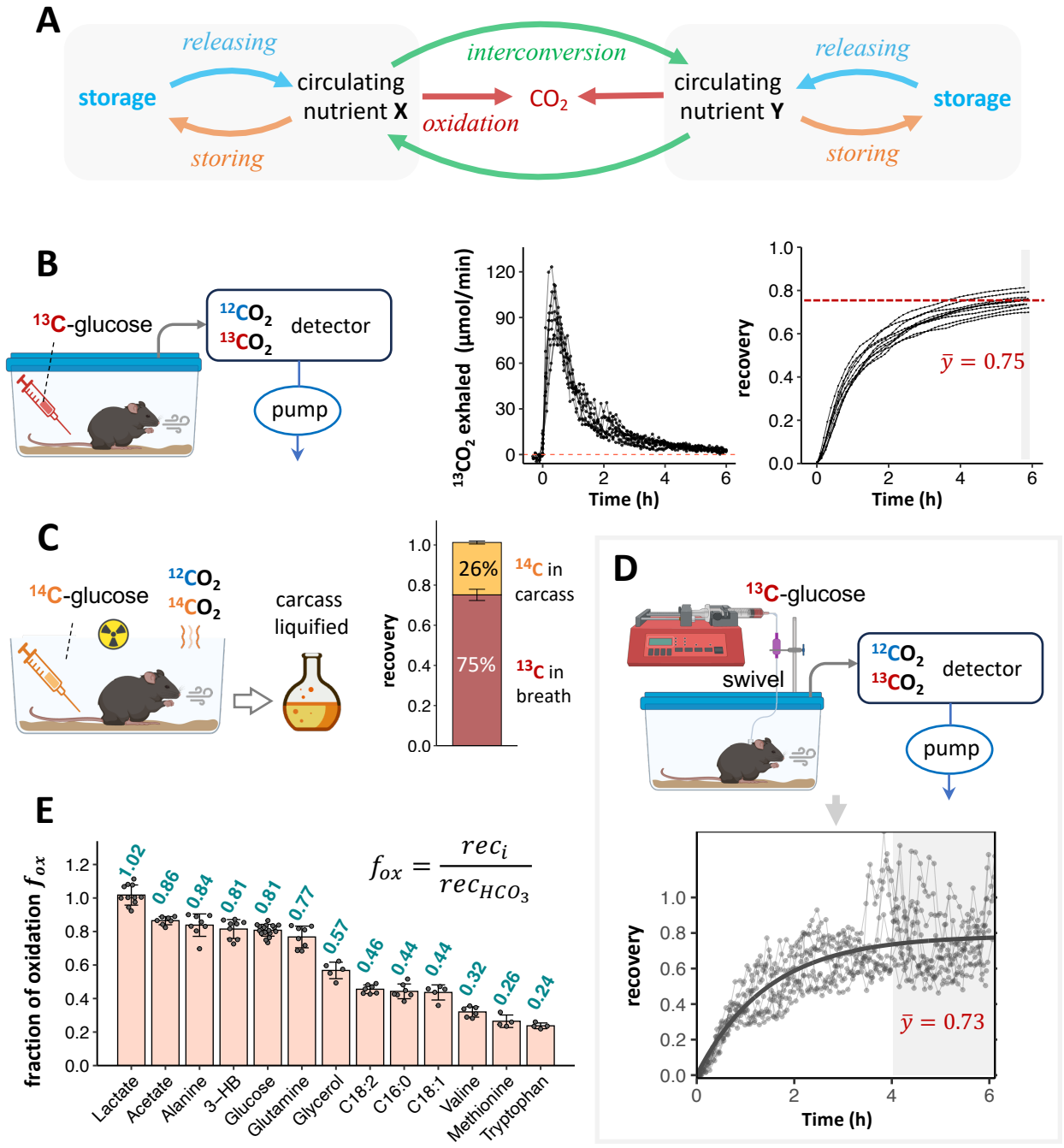

Figure 1. $^{13}CO_2$ Tracing Unveils Characteristic Oxidation and Storage Partition of Circulating Nutrients.

(A) Schematic of the releasing, storing, oxidation, and interconversion of circulating nutrients.

(B) Tracing of $^{13}CO_2$ production after intravenous (i.v.) injection of a nonperturbative bolus dose of ^{13}C-glucose. The $^{13}CO_2$ production kinetics (middle) and accumulated ^{13}C recovery (right)

are shown. Each line represents data from one animal. n = 10.

(C) Deposit of ^{14}C radioactivity in the carcass 6h later after i.v. injection of ^{14}C-glucose. n=3.

(D) Tracing of $^{13}CO_2$ production using nonperturbative i.v. infusion of ^{13}C-glucose in conscious unrestrained animal. Shown are the experimental setup (top) and ^{13}C recovery (bottom). Each thin line represents data from one animal and the thick line is fitted with formula $y = a \cdot (1 - e^{-b \cdot t})$. n = 10.

(E) Values of fraction of oxidation (f_{ox}) of 13 major circulating nutrients. Mean ± SD. n = 4 to 17 for individual nutrient, as noted in the scatterplot.

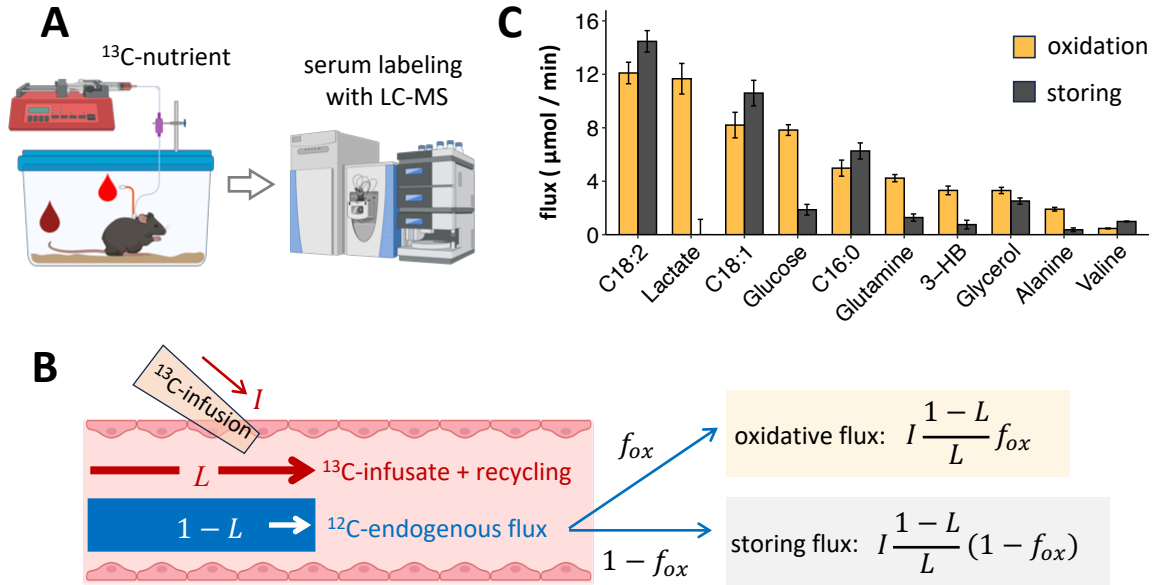

Figure 2. **Quantification of the Oxidation and Storing Fluxes of Circulating Nutrients.**

(A) Schematic showing infusion of ^{13}C-nutrient to mice and analysis of the serum labeling with LC-MS. Blood was collected from arterial blood via pre-implanted catheter and/or by tail snip.

(B) Illustration of the formula for calculating oxidation and storing fluxes of circulating nutrients. I, infusion rate of ^{13}C-nutrient; L, serum labeling of the infusate; and f_{ox}, fraction of oxidation, quantified in Figure 1.

(C) Oxidation and storing fluxes of major circulating nutrients. Mean ± SEM. For individual nutrient, for their labeling in serum, n = 4~15 (see Figure S3A); for f_{ox}, n = 4 to 17 (Figure 1E); the same replication applies to all figures computed from these two sets of parameters in Figures 2-5 and related supporting figures. Fluxes normalized by body weight refers to Figure S2C.

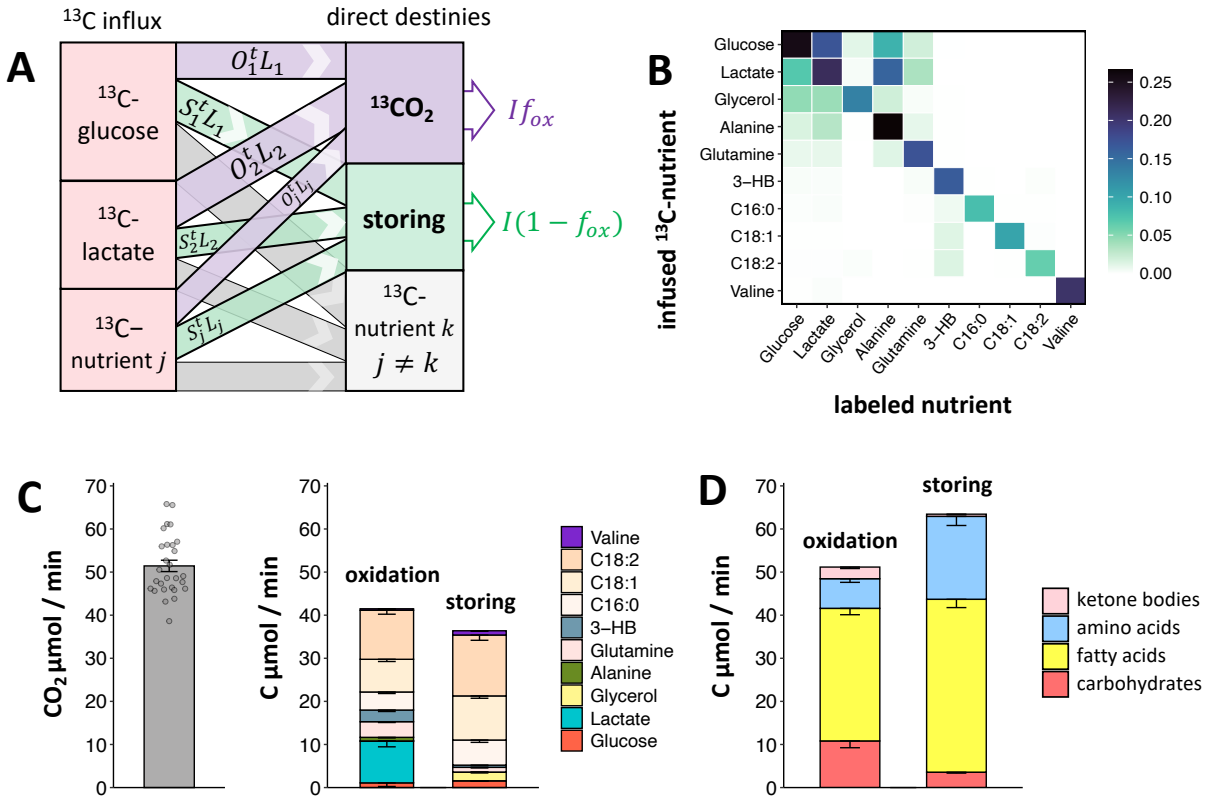

Figure 3. Quantification of *Direct* Oxidation and Storing Fluxes of Circulating Nutrients.

(A) Illustration for calculating direct oxidation and storing fluxes of circulating glucose. At the isotopic steady state of ^{13}C-glucose infusion, the total $^{13}CO_2$ production (oxidation) and storing flux of the ^{13}C-infusate are depicted as the sum of the direct oxidation and storing fluxes from all labeled circulating nutrients, respectively. O_j^t, S_j^t, and L_j are respectively the oxidation flux, storing flux (superscript t for total, including both ^{12}C and ^{13}C), and ^{13}C labeling of circulating nutrient j; f_{ox}, fraction of oxidation.

(B) Labeling of circulating nutrients under the infusion of different ^{13}C-nutrients. n = 4 to 15 for individual nutrient (see Figure S3A).

(C) Total CO_2 production (left, n = 28), in comparison with the direct oxidation and storing fluxes of the major circulating nutrients covered in this study (right).

(D) Direct oxidation and storing fluxes of all major circulating nutrients, including carbohydrates (glucose, lactate, and glycerol), fatty acids, protein-originated amino acids, and ketone bodies.

All data is presented in mean ± SEM. For panels (C-D), normalized fluxes by body weight refers to Figure S3C-D.

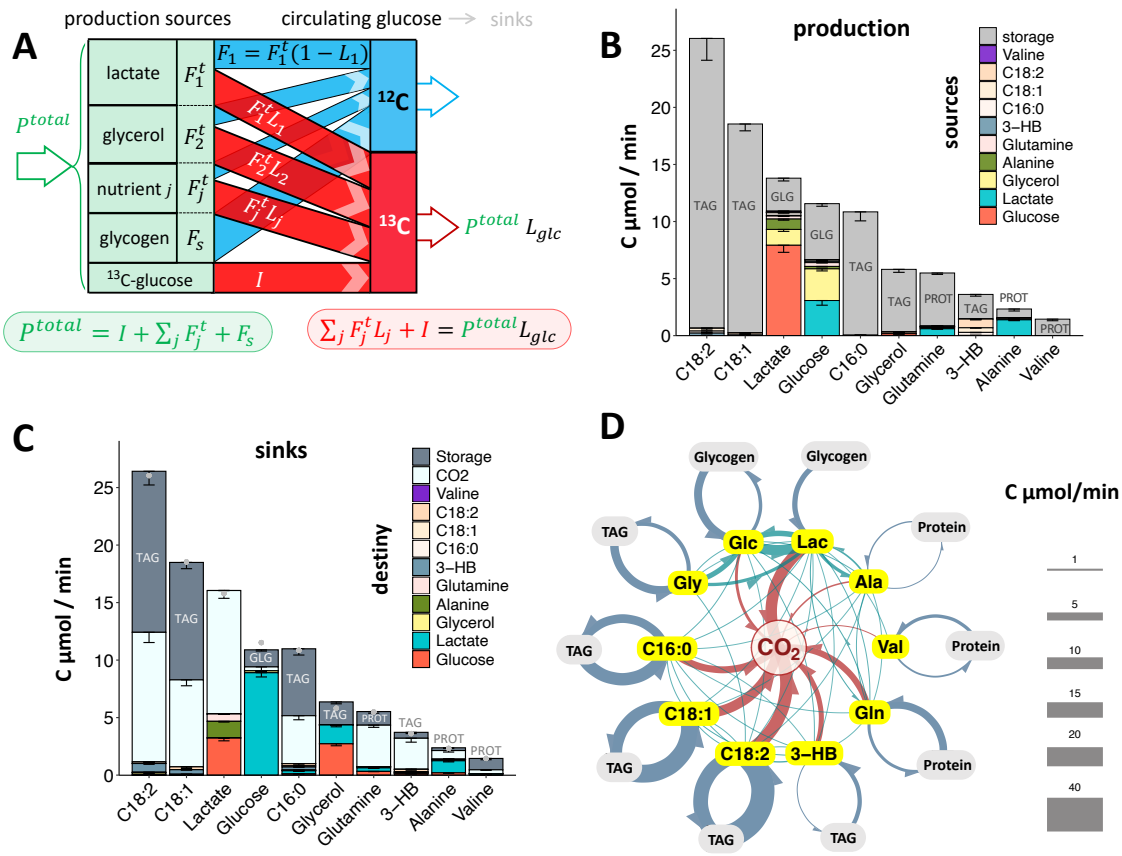

Figure 4. Quantifying Storage Releasing Flux and Interconverting Fluxes for Circulating Nutrients, and Integrating them with Oxidation and Storing Fluxes into a Holistic Flux Model of Circulating Nutrients.

(A) Illustration for calculating the storage releasing flux (glycogenolysis) and gluconeogenic fluxes to produce circulating glucose. I, the ^{13}C-glcose infusion rate; L_{glc}, the labeling of glucose; L_j, the labeling of nutrient j; F_j^t, the production flux from nutrient j to glucose, superscript t for total (including both ^{12}C and ^{13}C); F_s, the releasing flux from storage of glycogen.

(B) The production fluxes of circulating nutrients from storage and other circulating nutrients. TAG, triglyceride; GLG, glycogen, PROT, protein.

(C) Sink fluxes of circulating nutrients, fated to oxidation, storage, and other circulating nutrients. The dot shows the total production flux as quantified in Figure 4B. For panels (B) and (C), fluxes normalized by body mass refers to Figure S4 A-B.

(D) An organism-level metabolic map of circulating nutrients. All flux arrows are drawn in counter-clockwise direction. All data is presented in mean ± SEM.

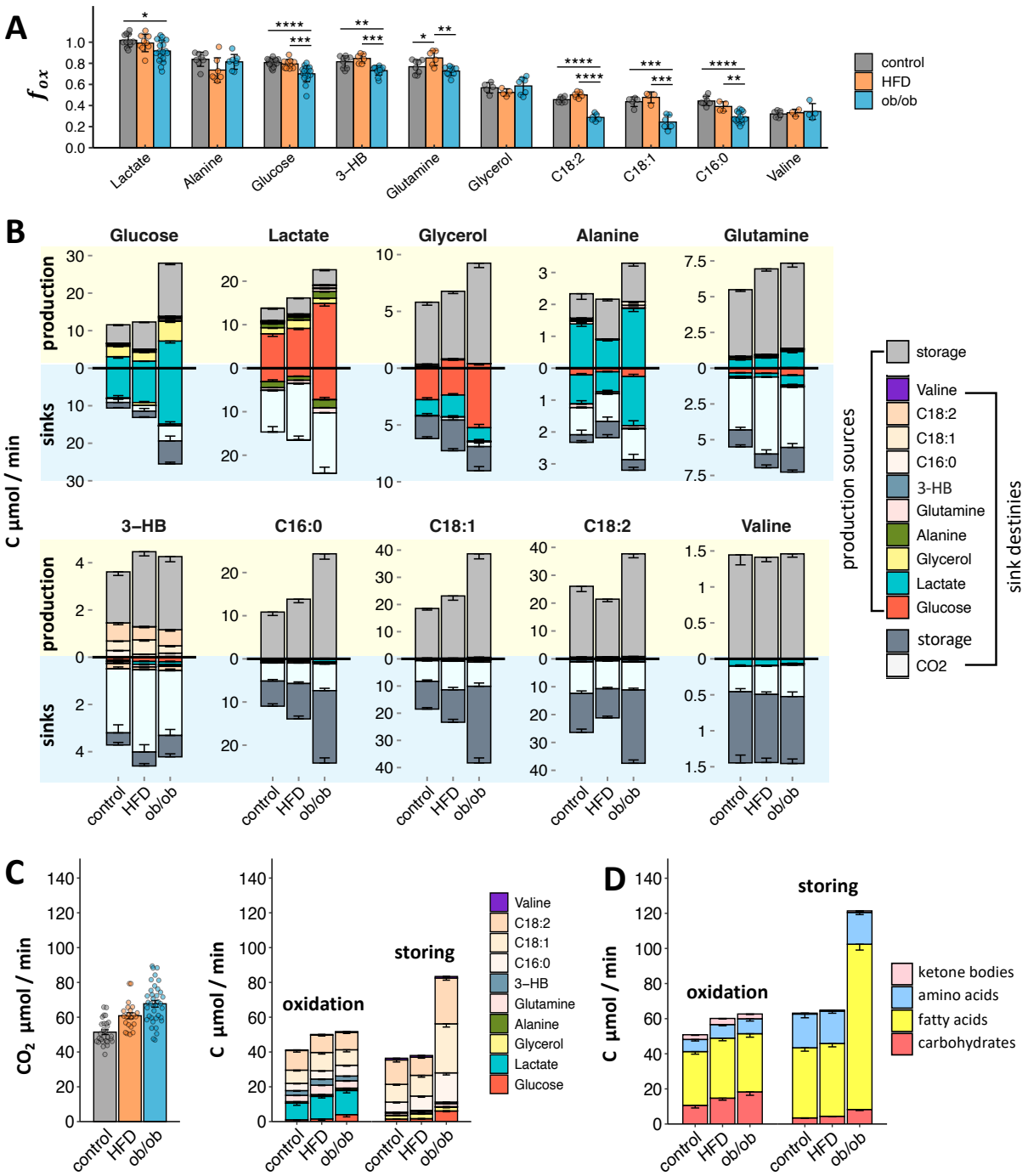

Figure 5. Systematic Flux analysis of Circulating Nutrients in High Fat Diet- Fed (HFD) and ob/ob Mice

(A) Fraction of oxidation (f_{ox}) of circulating nutrients in chow-fed wild type control mice, and the obese mice. Mean ± SD.

(B) Production and sink fluxes of circulating nutrients in the control and obese mice.

846 **(C)** Total CO_2 production (left), and the direct oxidation and storing fluxes of circulating
847 nutrients (right) in the control and obese mice.
848 **(D)** Direct oxidation and storing fluxes of all major circulating nutrients, including
849 carbohydrates (glucose, lactate, and glycerol), fatty acids, protein-originated amino acids, and
850 ketone bodies.
851 Fluxes normalized by lean or body mass refers to Figure S6B. All data is presented as mean ± SEM
852 unless otherwise specified. *p < 0.05, **p < 0.01, ***p<0.001, ****p<0.0001 by Student's t test
853 after Bonferroni adjustment. Regarding individual nutrient and phenotype, for f_{ox}, n = 3 to 19
854 (see scatterplot in panel A); their labeling in serum, n = 4 to 27 (see Figure S6A). The same
855 replication also applies to the related supporting figures.
856

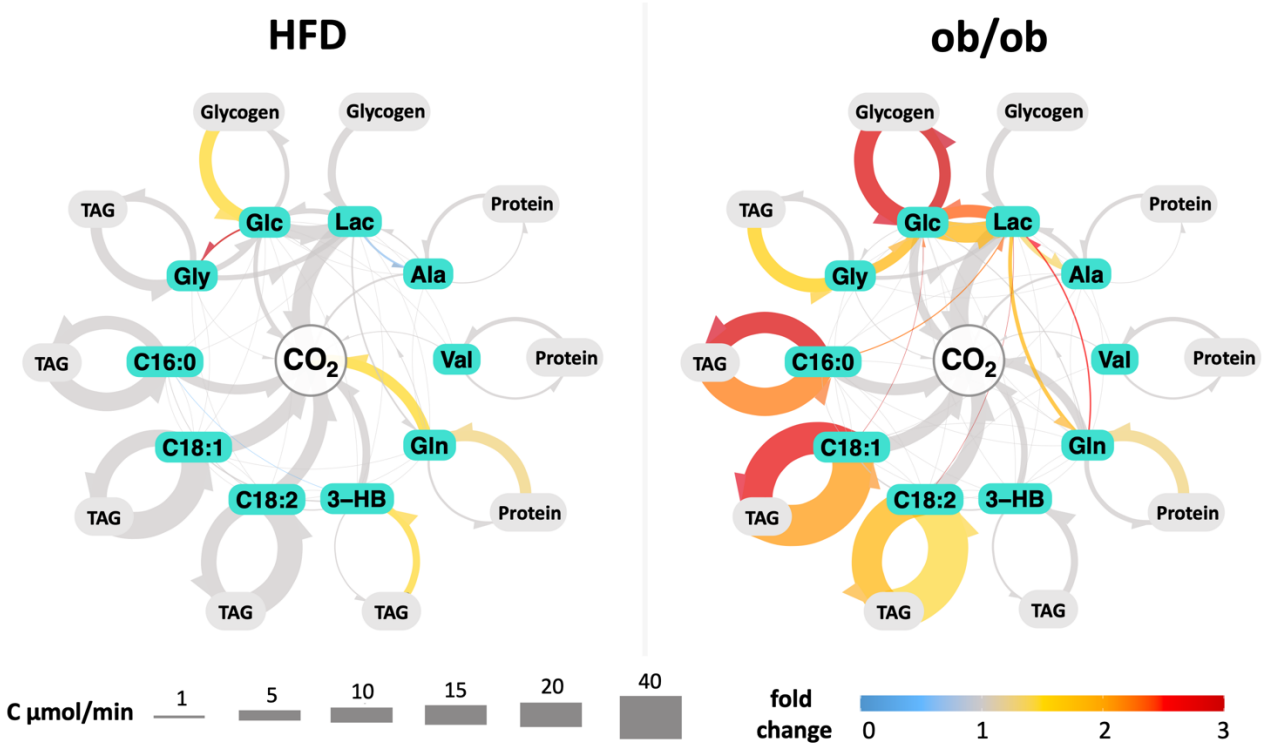

857

858 **Figure 6. Flux Models of Obese Mice Reveals Elevated Metabolic Cycling in ob/ob Mice, but Not**

859 **in High Fat Diet-Fed Mice.**

860 Fluxes in obese mice that are statistically significant (Bonferroni-adjusted *p* value < 0.05) from

861 the control mice are highlighted in color, with fold change mapped to the color scale. All flux

862 arrows are drawn in counter-clockwise direction.

863